remote sensing

MDPI

Article

Sea Tide Influence on Ice Flow of David Drygalski's Ice Tongue Inferred from Geodetic GNSS Observations and SAR Offset Tracking Analysis

Luca Vittuari [1], Antonio Zanutta [1,*], Andrea Lugli [1], Leonardo Martelli [2] and Marco Dubbini [3]

[1] Department of Civil, Chemical, Environmental and Materials Engineering, University of Bologna, Viale Risorgimento 2, 40136 Bologna, Italy; luca.vittuari@unibo.it (L.V.); andrea.lugli8@unibo.it (A.L.)
[2] Istituto Nazionale di Geofisica e Vulcanologia (INGV)—Viale Carlo Berti Pichat, 6/2, 40127 Bologna, Italy; leonardo.martelli@ingv.it
[3] Department of History and Cultures, University of Bologna, Via Guerrazzi 20, 40124 Bologna, Italy; marco.dubbini@unibo.it
* Correspondence: antonio.zanutta@unibo.it

Abstract: David Glacier and Drygalski Ice Tongue are massive glaciers in Victoria Land, Antarctica. The ice from the East Antarctic Ice Sheet is drained through the former, and then discharged into the western Ross Sea through the latter. David Drygalski is the largest outlet glacier in Northern Victoria Land, floating kilometers out to sea. The floating and grounded part of the David Glacier are the main focus of this article. During the XXI Italian Antarctic Expedition (2005–2006), within the framework of the National Antarctic Research Programme (PNRA), two GNSS stations were installed at different points: the first close to the grounding line of David Glacier, and the second approximately 40 km downstream of the first one. Simultaneous data logging was performed by both GNSS stations for 24 days. In the latest data processing, the kinematic PPP technique was adopted to evaluate the dominant diurnal components and the very small semi-diurnal variations in ice motion induced by the ocean tide and the mean ice flow rates of both GNSS stations. Comparison of the GNSS time series with predicted ocean tide calculated from harmonic coefficients of the nearest tide gauge stations, installed at Cape Roberts and Mario Zucchelli Station, highlight different local response of the glacier to ocean tide, with a minor amplitude of vertical motion at a point partially anchored at the bedrock close to the grounding line. During low tide, the velocity of the ice flow reaches its daily maximum, in accordance with the direction of seawater outflow from the fjord into the ocean, while the greatest daily tidal excursion generates an increase in the horizontal ice flow velocity. With the aim to extend the analysis in spatial terms, five COSMO-SkyMED Stripmap scenes were processed. The comparison of the co-registered offset tracking rates, obtained from SAR images, with the GNSS estimation shows good agreement.

Keywords: Antarctic glaciology; kinematic precise point positioning; GNSS time series; ice dynamics; synthetic aperture radar; COSMO-SkyMed

Citation: Vittuari, L.; Zanutta, A.; Lugli, A.; Martelli, L.; Dubbini, M. Sea Tide Influence on Ice Flow of David Drygalski's Ice Tongue Inferred from Geodetic GNSS Observations and SAR Offset Tracking Analysis. *Remote Sens.* **2023**, *15*, 2037. https://doi.org/10.3390/rs15082037

Academic Editors: Gonçalo Prates and Manuel Berrocoso Domínguez

Received: 20 February 2023
Revised: 5 April 2023
Accepted: 10 April 2023
Published: 12 April 2023

1. Introduction

David Glacier is the largest outlet glacier in Northern Victoria Land, collecting a catchment area of approximately 4% of East Antarctica [1]. Its basin extends to Dome C and Talos Dome and produces a floating ice tongue of about 140 km long from the grounding zone and about 20 km wide, with 90 km of longitudinal extent not extending into the Ross Sea. As most of David Glacier basin is below the sea level, it is a marine-based glacier, with the grounding line about 2000 m below the sea level [2,3]. Basal melting at the grounding line position is estimated at 29 ± 6 m ice/yr [1,2]. Further downstream, basal melting decreases by a factor of two. Due to its size, the David-Drygalski ice system affects local ocean circulation and the persistence of the polynya within Terra Nova Bay. At the point

where the David Glacier crosses the Transantarctic Mountains, there is a steep change in slope of the basal topography of the glacier, which generates an icefall, the so-called David Cauldron, not far from the area in which it is assumed the grounding line occurs [4]. The David-Drygalski has been studied for a long time, since the early 1990s [2,5–15]. Current studies on the coupling between glaciers and bedrock identify the prevailing processes by which ice flows onto the bedrock before arriving at the grounding zone; these are regeneration and plastic flow. Danesi et al. [16] observed an intense seismicity, clustered in time and space, at the base of the David Cauldron, which abruptly stopped after 2004; between 2003 and 2016 two significant seismic clusters were recorded upstream of the icefall, which highlighted the influence of basal lubrication conditions on seismic events. Finally, they observed at the end of 2003 a strong correlation between the sea tide and the icequake time series with a period of 14 days. The latter was analyzed in Vittuari et al. [17], and it was found to be the period of passage of the moon at the equator that forces the variation in the amplitude of the sea tide in the area and influences the horizontal velocity of the ice flow. Moon et al. [14], through a 3-year observation derived by synthetic aperture radar (SAR) offset tracking observations, show that the velocity observed astride the David Cauldron tends to increase during the Antarctic summer. The geodetic monitoring of the floating and grounded parts of the David Glacier can underline how much the GNSS data collected and well documented in the past can provide useful information today for further studies and evaluations, thanks to the advancement of analysis techniques.

In this study, we employed recent GNSS post-processing techniques using the kinematic precise point positioning (KPPP) undifferentiated approach. The latter was applied on two datasets, each lasting 24 days, collected in 2006, close to the grounding line and downstream of it. In this paper, two lines are reported: the first defined within the Polar Year Project ASAID [4], and the second within the Project MEaSUREs Antarctic Grounding Line from Differential Satellite Radar Interferometry, Version 2 [18–20].

One of the strengths of the method is that of being able to compare, in a very detailed way, daily signals coming from receivers placed in very different positions on the David Glacier, thus highlighting the influence of the tide on its horizontal and vertical movements. The spatial analysis was then extended using synthetic aperture radar (SAR), through the processing of three pairs of Cosmo-SkyMED Stripmap scenes. This makes it possible to evaluate the variations in the daily velocity of the ice flow over a period of fifteen days, considering the cycle induced in the ocean tide by the passage of the moon at the equator.

The fact that the David Glacier is a marine-based glacier means that it is particularly sensitive to changes in ocean conditions, such as warming ocean temperatures or the influx of warm water from currents. Understanding the behavior and response of marine-based glaciers like the David Glacier is an important area of research in understanding the impacts of climate change on the Antarctic Ice Sheet.

2. Ice Flow Derived by Geodetic GNSS Observations

The David Glacier has two major feed streams: the main southern flow from Dome Circe and the slower-moving northern flow from Talos Dome, which merge. In this paper, the control points are located only within the southern flow and no information can be extracted from this analysis about the northern flow. To understand some characteristics of the dynamics of the southern ice flow and the effect of the ocean tide on the movements of the floating and grounded parts of David Glacier, two dual-frequency GNSS geodetic receivers were installed on its surface at the end of 2006. These stations have become part of an observation network of seismic stations already operating in the study area [21].

To accomplish the above, the first station was installed at ICF1, close to the area where the flotation zone of David Glacier is assumed to start, and the second station was at DRY1, approximately 40 km downstream of ICF1 and 100 km from the edge of the Ross Sea (Figure 1). Unfortunately, when the experiment was set up, the GNSS master station, installed on a rocky outcrop near the ice tongue, for some unidentified reason, stopped acquiring after a few days of operation. To overcome the problem, some satisfactory results

have been achieved in post-processing, adopting the double difference technique, using data from a permanent GNSS station (TNB1), about 100 km away from the study area, at the Mario Zucchelli station (MZS) [21].

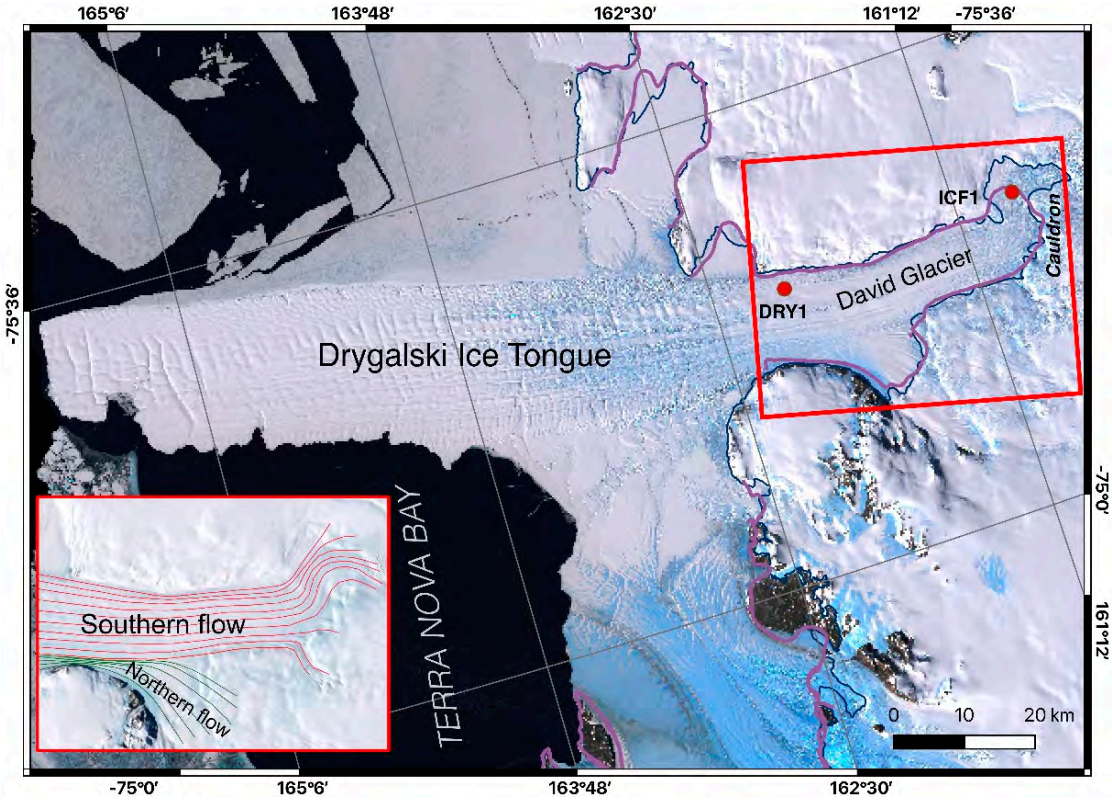

Figure 1. Terminal part of the David Glacier and the floating Drygalski Ice Tongue (USGS—LIMA Landsat high-resolution virtual mosaic). Red dots are the positions of the temporary GNSS stations ICF1 and DRY1. Two interpretations of the grounding line are reported in the figure: (blue) grounding line extracted from ASAID [4], (purple) grounding line described by the Project MEaSUREs Antarctic Grounding Line from Differential Satellite Radar Interferometry, Version 2. Both GNSS stations collected data simultaneously for 24 days in 2006, from 15 January 15 to 7 February. In the detail box inside the figure, the two main ice flows (southern and northern) are indicated with dashed red and green lines, respectively [6].

Nowadays, the undifferenced GNSS post-processing analysis technique (Precise Point Positioning), together with the recent improvements available for the kinematic reconstruction of the position of a single GNSS instrument, with a sampling rate of even less than one minute, allow a detailed reanalysis of such data, highlighting signals that were not detectable with the analysis techniques used at the time of the experiment.

Reference [17] includes comparisons between a double-difference approach using the Track Gamit-Globk software and the undifferentiated PPP approach using the Bernese GNSS software, Version 5.2. Given the distance of about 100 km from the reference station located on granite outcrops at Mario Zucchelli Station, the second solution is less noisy and does not have outliers that can reach and exceed one meter, which are present in the first solution. Some specifics on GNSS monumentation are provided here, as it is an important aspect of any geodetic installation, especially one built on a moving ice body with temperatures and winds varying suddenly and rapidly. The procedure that follows was repeated for each installation point. Starting from previous experience with GNSS measurements in similar conditions, a 3 m long aluminum pole of about 13 cm diameter was driven about one meter into the ice at the chosen position (Figure 2). A hollow aluminum pole with a diameter sufficient to counteract vertical oscillations has two great advantages

compared with other types of materials. Since the thickness of the metal is only a few mm, it is very light and tends to cool down and anchor itself very efficiently to the ice in which it is fixed, as it anchors very strongly inside and outside the circular section. Moreover, the variation in the length of pole due to the thermal expansion (26.3×10^{-6} m per meter per Celsius degree) can be considered negligible. Then, a self-centering device was inserted at the top of the pole to fix the GNSS antenna.

(**A**) (**B**)

Figure 2. (**A**) DRY1 semi-permanent GNSS station monumented on ice; (**B**) anchoring the instrument box and the solar panel to a dead body buried in the ice.

Each instrument system was powered by two batteries recharged by solar panels. Since the installation points were reached by helicopter, the size and weight of the GNSS station facilities were designed to be easily transported considering the space available inside the Squirrel helicopter and in the basket placed above the skid.

Two GNSS units were used for the survey, each composed of a Trimble 5700 geodetic receiver equipped with a Trimble Zephyr antenna; the sampling rate of the raw acquisitions was fixed at 15 s. The GNSS receiver, together with the batteries and the electronic control unit, were placed inside insulated boxes to protect the instrumentation from temperature and ice. The collected GNSS data was then processed using the Precise Point Positioning (PPP) approach, implemented in the Bernese V5.2 software [22], to obtain a kinematic averaged solution every 5 min.

The PPP technique allows the position of a single receiver to be determined with centimeter-level accuracy [23], using undifferenced dual-frequency code and phase observations, whether the phase ambiguity resolution was successful. CODE/IGS products such as satellite orbits, Earth orientation parameters (EOP), satellite clock corrections, and absolute antenna phase center variation (PCV) models were used in the calculation, together with IGS products for the atmosphere modeling. Solid Earth tides, Earth rotation, and ocean tidal loading were applied according to IERS 2010 Conventions [24]. PPP processing implies ionosphere-free combinations of multifrequency pseudorange and carrier-phase observations to estimate the unknown parameters by fixing satellite coordinates and satellite clock parameters. Receiver coordinates, the troposphere, carrier phase ambiguities, and the receivers' clock parameters were estimated in a consistent way with respect to the global reference system defined by the satellite ephemerides and the ancillary products.

The PPP processing was part of an automated pipeline that starting from the daily observations to produce the estimate of the coordinates based on the user-defined kinematic sampling interval. To achieve the desired result, some modifications were made to the software, in particular to the client Perl scripts, in order to manage high-frequency outputs. The results were processed through Perl scripts and Fortran95 routines to obtain input files for the Matlab Tsview software [25] used for interactive time series analysis.

The result of the GNSS data processing is the estimation of the geocentric Cartesian coordinates of stations and their uncertainties expressed within the International Terrestrial Reference Frame 2014 (ITRF2014). The Cartesian coordinates were then converted to a local

geodetic coordinate system (North, East, and Up). The time series of the local geodetic coordinates for both stations are shown in Figure 3, where the trends of the North and East components represent the horizontal velocity of the ice flow, while the Up component represents the vertical motion measured during the 24 days of observation.

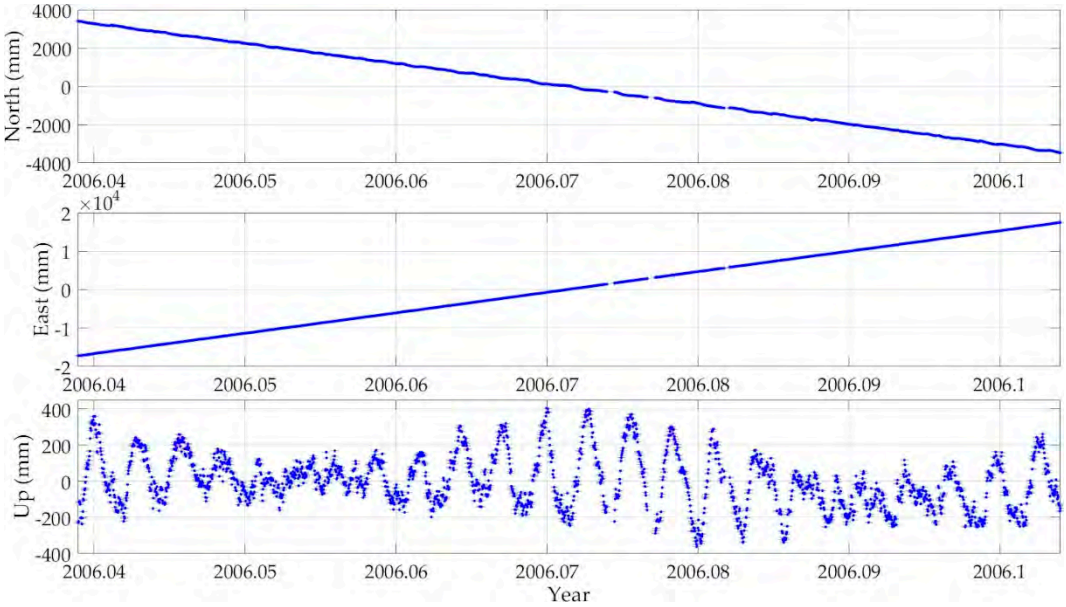

(**A**)

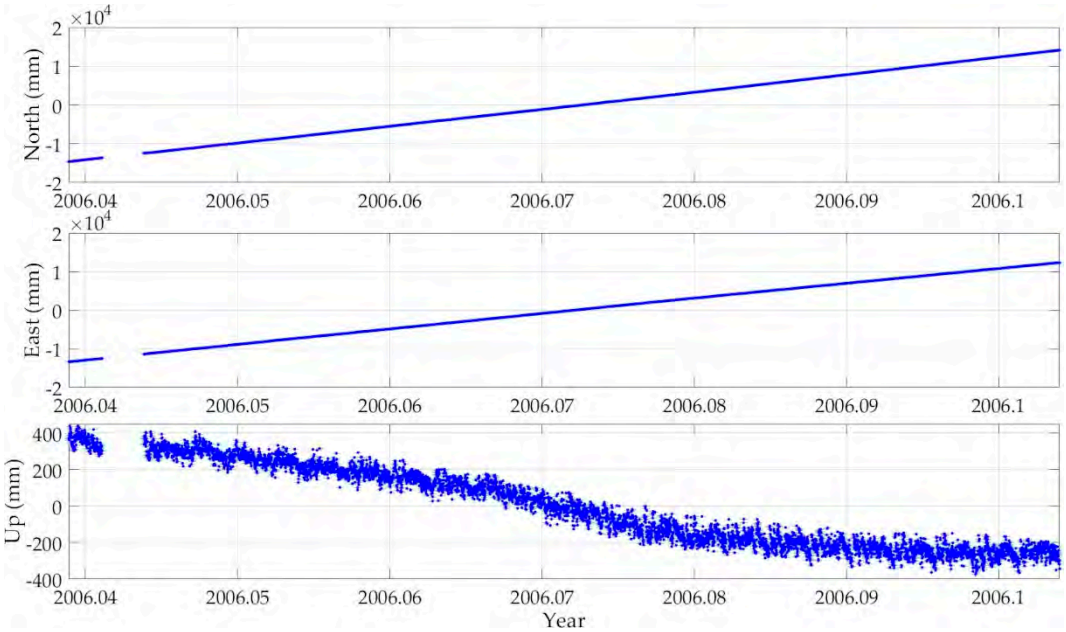

(**B**)

Figure 3. Local geodetic coordinate system time series of GNSS stations DRY1 (**A**) and ICF1 (**B**); time scale in years.

The open-source software Tsview, a MatLab program for interactive analysis of the time series based on the least squares fitting technique [26,27], was used to estimate linear trends and residual detrended coordinates of time series. The station velocities were then estimated individually for each component from the station position time series.

An interactive inspection of time series was performed to remove some outliers, followed by an automatic outlier rejection using the 3-sigma criterion. The RealSigma

noise correlation model implemented in Tsview was used to account for the influence of time-correlated effects in estimating the confidence intervals of the velocity components; finally, the residual time series was estimated after subtracting the trend (Figure 4, Table 1).

Table 1. Estimated coordinates and horizontal velocities of GNSS stations. Velocities and errors are in m/yr.

ID	Lon (°)	Lat (°)	H (m)	Ve	$\pm\sigma_e$	Vn	$\pm\sigma_n$	Ven	$\pm\sigma_{en}$
DRY1	162.1446813	−75.3624533	36.330	533.151	0.029	−105.295	0.024	543.447	0.026
ICF1	160.9012510	−75.3854408	201.798	394.607	0.056	441.290	0.063	591.964	0.021

Spectral analysis of GNSS time series provides a very powerful tool for understanding signals due to the intrinsic mechanism affecting the movements of the stations [26]. This results in an intuitive means of determining the period of oscillation, but, unfortunately, the total sampling period of 24 days is not long enough to estimate the interesting frequency of 14 days due to the passage of the moon at the equator. Furthermore, the spectral analysis of NEU components was performed only on shorter periods, due to the main diurnal and small semi-diurnal components of the ocean tide, using the Lomb-Scargle periodogram [27–29], a statistical tool which can detect and characterize periodic signals in unevenly sampled data. This method evaluates the time series data at the measured time and reconstructs the missing values from the amplitude and phase information of the dominant frequencies, without performing any interpolation [30]. The results of the analyses are presented in Figures 4–7 and in Table 2.

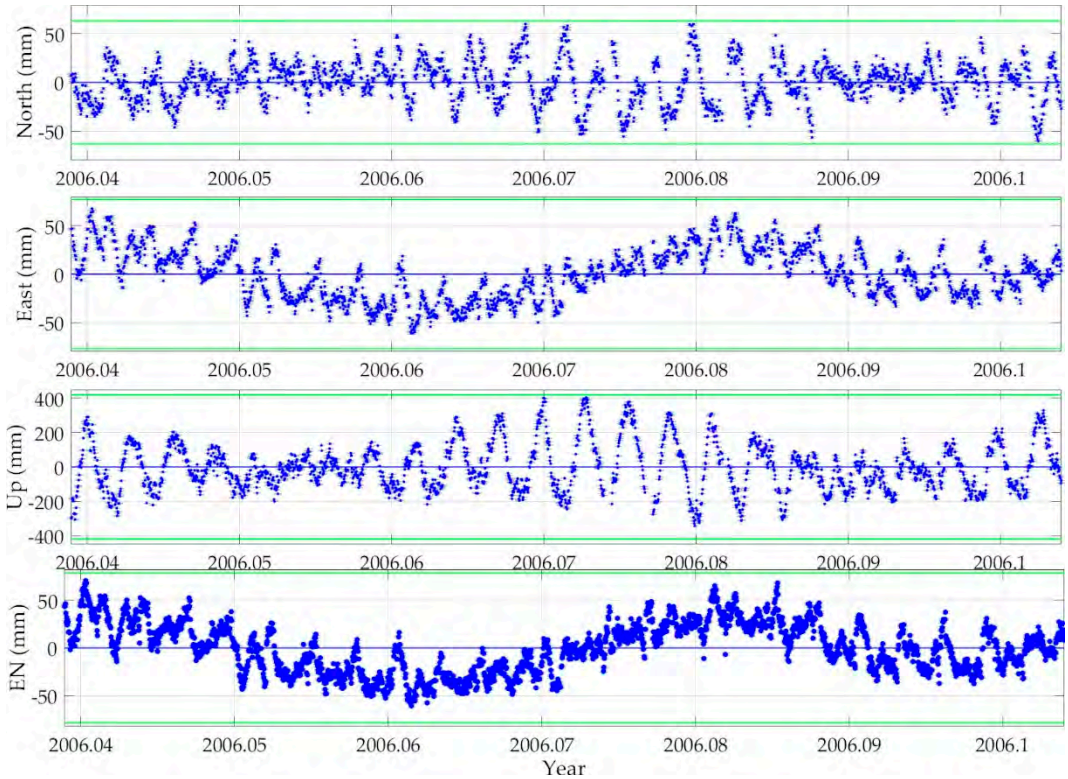

(A)

Figure 4. *Cont.*

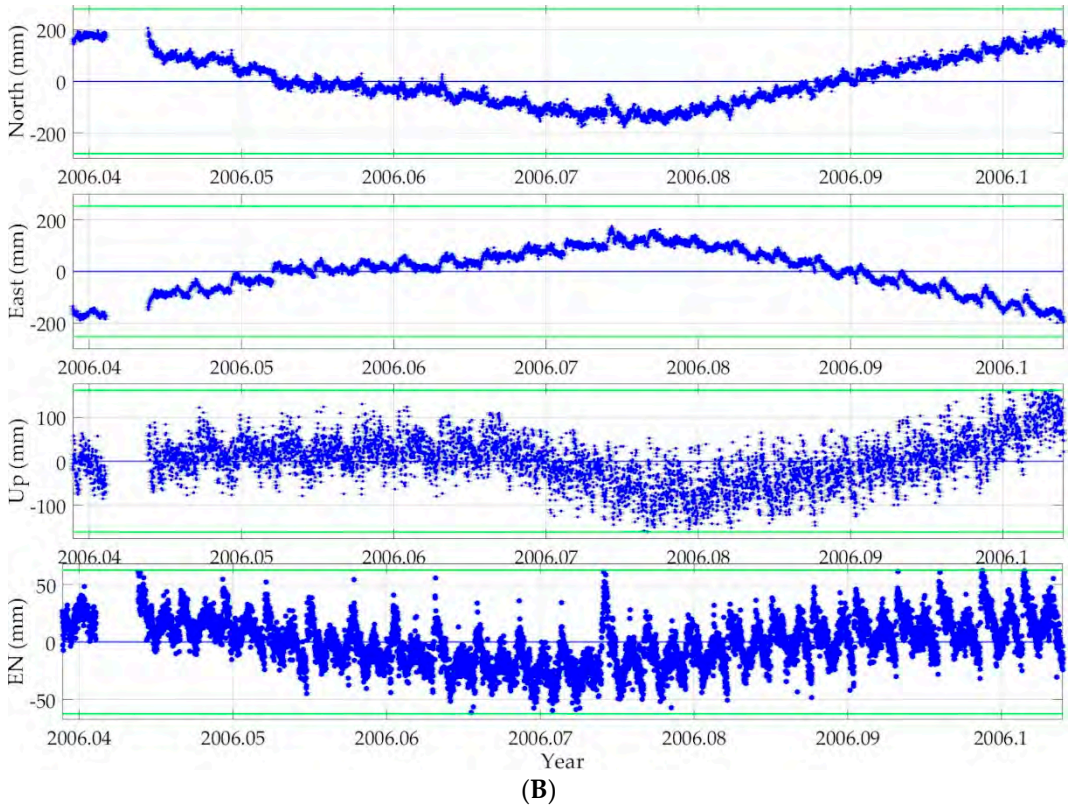

Figure 4. Detrended time series of DRY1 (**A**) and ICF1 (**B**) GNSS stations. The residuals of N, E, U, and horizontal EN components are evaluated removing the linear trend. The green horizontal lines show the bounds of 3-times the WRMS scatter of the residuals. For point DRY1, the response to the estimated ocean tide in the Up component is clear; concerning the signals evidenced by the North, East, and East-North plots, the increment in the horizontal ice flow velocity with the increment in the amplitude of the ocean tide pointed out by the horizontal component EN is clear.

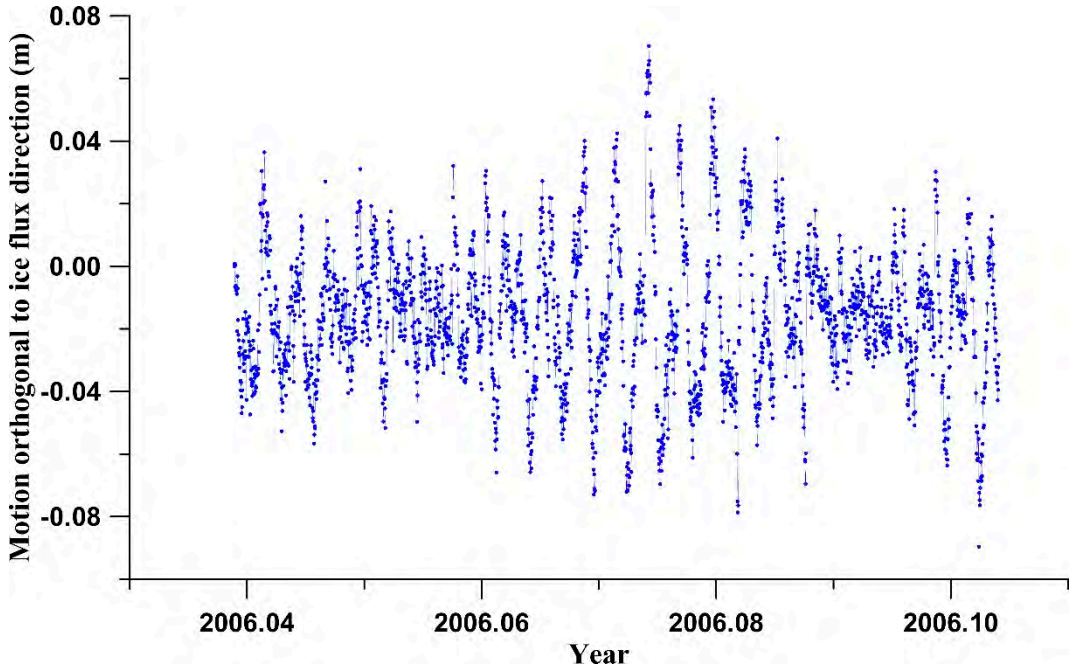

Figure 5. Motion across the ice flow direction at point DRY1.

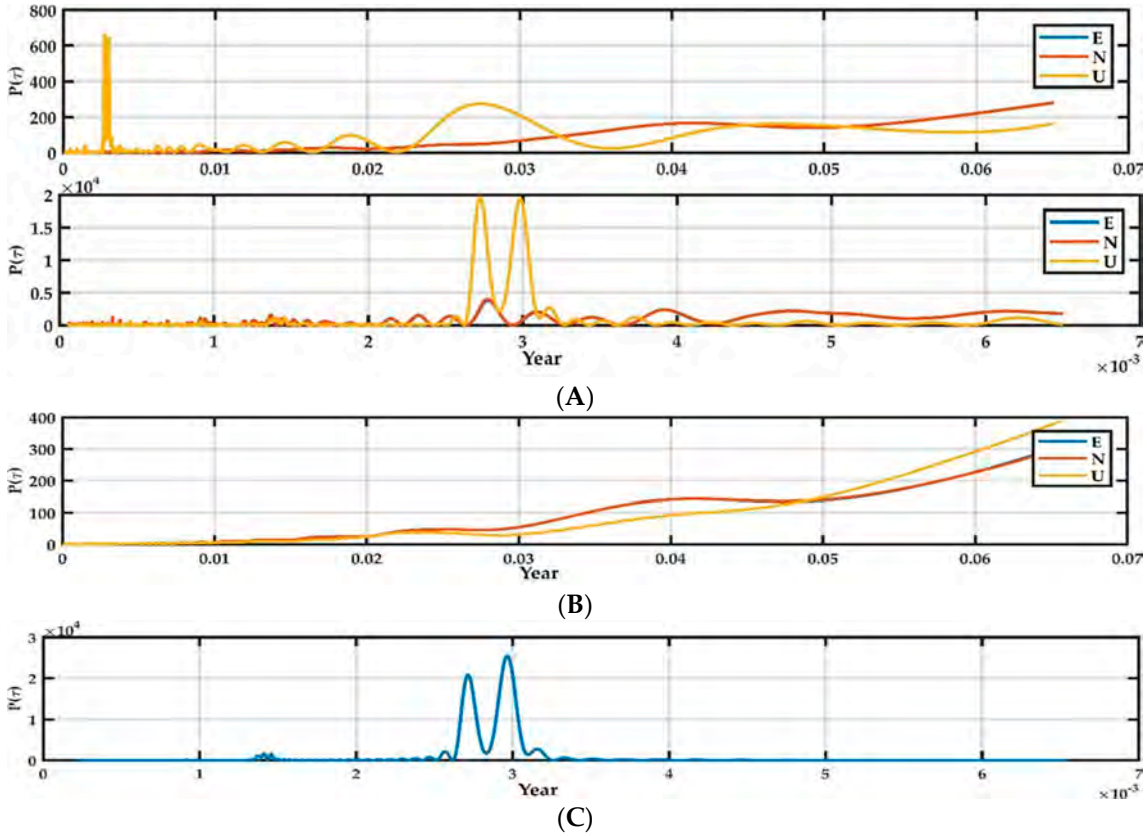

Figure 6. Lomb–Scargle periodograms computed for DRY1 (**A**, **top**) and ICF1 (**B**) GNSS time series, separately for each coordinate component. Figure (**A**, **bottom**) shows a zoom of the region near the peak (1×10^{-3} y = 8.76 h) of the DRY1 analysis. Figure (**C**) shows the same analysis of the Up component of the predicted ocean tide at Mario Zucchelli Station (MZS) obtained by harmonic coefficients available in the ATG database. The ordinates show Lomb-Scargle Power, the abscissa the period (0.01 y = 3.65 days).

Table 2. Estimated most significant parameters coming from the spectral analysis of the DRY1 and predicted ocean tide time series.

Component	Amplitude (m)	Phase (°)	MSE * (m)
	DRY1 T1 = 0.00272691 y, 23.9 h		
U	0.126	22.6	0.066
	DRY 1 T2 = 0.00298356 y, 26.1 h		
U	0.123	−52.6	0.066
	Predicted ocean tide T1 = 0.0029633 y, 26.0 h		
U	0.206	98.1	0.024
	Predicted ocean tide T2 = 0.00271067 y, 23.7 h		
U	0.186	−42.3	0.028

* MSE Mean Squared Error.

The nonlinear motion of the ice flow evidenced by the North component was investigated in more detail, by projecting the components of motion along and across the ice flow direction at DRY1, because the magnitude of the component was not explainable by a simple oscillation of the aluminum pole induced by the ocean tide. In Figure 5 are reported the components across the ice flow azimuth of 101.17°, measured from the motion profile at the point. Figure 6 shows the periodograms obtained for time series of both GNSS stations compared with the synthetic ocean tide prediction data.

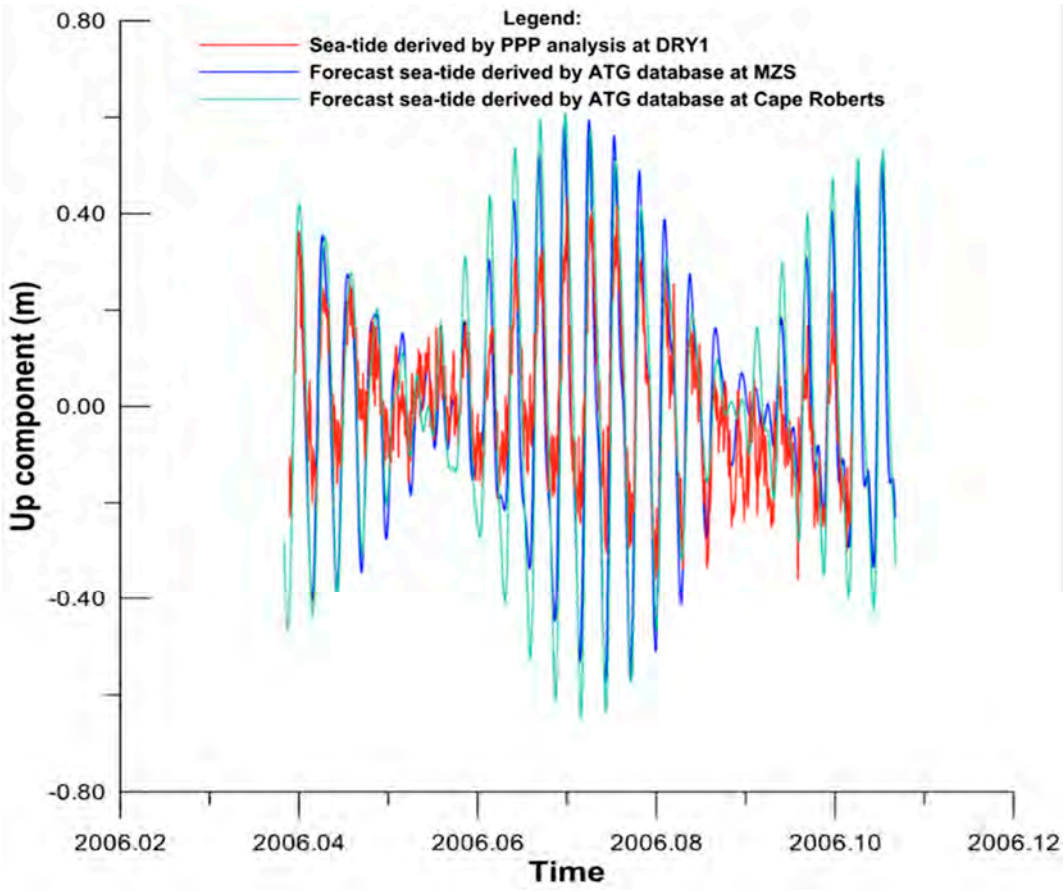

Figure 7. Comparison between the time series of the Up component obtained from the PPP calculation of the GNSS observations acquired at DRY1 and the predicted ocean-tide calculated from Q1, O1, P1, K1, N2, M2, S2, K2 harmonic coefficients published in the ATG database for two sites: MZS (about 100 km north of DRY1) and Cape Roberts (about 170 km south of DRY1). The diurnal declinational tides K1 and O1 are the most important tides, which occur once a day. In the Ross Sea, as well as in the coasts between 65°W to 140°E, there is a tide cycle per day; the lunar phases almost do not affect the tides. This confirms Thiel et al. [31], who first showed that the Ross Sea tide is diurnal and that the solar component predominates.

Concerning point ICF1, the horizontal component EN points out a curved motion of the ice flow where the pole was fixed, and an interesting movement with a saddle shape is evidenced by the Up component.

An important effect that is expected to be present in the David Drygalski movements is the response to ocean wave stresses. However, these vibration resonance frequencies, described, for example, for the ice tongue of the Mertz glacier, are on the order of 10s [32]. This is too short a period to be highlighted by the spectral analysis described above, due to the sampling rate of the GNSS measurements analyzed.

3. SAR Data Analysis

Although the GNSS time series analysis is very accurate, it refers to isolated points, and therefore it was considered interesting to broaden the analysis in spatial terms also, using synthetic aperture radar (SAR). The processed dataset analyzed consists of 5 Cosmo-SkyMED Stripmap scenes (in the following CSK), made available by the Italian Spatial Agency (ASI) in the framework of the Announcement of Opportunity 2288.

The CSK sensor acquired in X band, with a wavelength of 3.1 cm, and a nominal spacing of 1.54 × 2.35 m, respectively, in range and azimuth. These scenes were acquired in

descending geometry from August to September 2009, allowing the formation of three pairs, each with a temporal baseline of 8 days (Table 3).

Table 3. The three processed SAR pairs numbered in temporal order.

Pair Number	Master	Slave	Height of Ambiguity (m)
I	16-08-2009	24-08-2009	177
Scene ID	CSKS1_SCS_B_HI_06_HH_LD_SF_2009 0816061506_20090816061512	CSKS2_SCS_B_HI_06_HH_LD_SF_2009 0824061501_20090824061507	
II	24-08-2009	01-09-2009	188
Scene ID	CSKS2_SCS_B_HI_06_HH_LD_SF_2009 0824061501_20090824061507	CSKS1_SCS_B_HI_06_HH_LD_SF_200909 01061456_20090901061502	
III	17-09-2009	25-09-2009	187
Scene ID	CSKS1_SCS_B_HI_06_HH_LD_SF_2009 0917061445_20090917061451	CSKS2_SCS_B_HI_06_HH_LD_SF_200909 25061439_20090925061445	

Due to the high differential kinematics of the glacier (faster at the center than at the sides, with stable rocky outcrops on the flanks), it is arduous to retrieve displacement velocities considering the unwrapped SAR phase, because of the lack of both sufficient coherence (even with a short temporal baseline) and of reliable ground control points for phase calibration.

An alternative approach is coregistration offset tracking (coherence tracking), less accurate than InSAR but with the benefit of also allowing observation in the azimuth direction [33].

All the pairs were processed with a DEM-assisted coregistration [34], considering a DEM previously obtained by processing two ERS tandem pairs (in the framework of ESA Cat.1 project 5410), whose height accuracy and spatial sampling have been deemed suitable to avoid topographic residuals. To mitigate errors related to acquisition geometry, offsets along the glacier were calibrated applying polynomials whose coefficients were estimated through a least square regression of "stable" point offsets (e.g., rocky outcrops where high coherence was retained). In summary, since glacier offsets are expressions of both ice velocities and errors, considering stable point offsets allows splitting these two components (for a review of this technique refer to Liu et al., [35]).

In general, the precision of tracking-based methods depends on the pixel dimensions: in case of SAR coherence tracking, for the image-patch sizes and oversampling factors considered in this study, the accuracy is of about 1/20 of pixel dimension. The precision of the displacement vector can be approximated to the sum of the accuracies in ground-range and azimuth directions, so, a value referring to a single day is given by the division by the number of days between the two acquisitions [33]. Knowing the acquisition geometry, local topography, and simulated tide heights, it is possible to decompose the displacement vector into its horizontal and vertical components [36]. Regarding the subsequent processing, we considered only the horizontal component. Offsets have been interpolated with a natural neighbor algorithm to get a continuous map of the glacier velocity field; then the obtained grids were validated in a GIS environment, comparing the obtained results with respect to the velocities reported in the MEaSUREs InSAR-Based Antarctica Ice Velocity Map, Version 2 [13,18,37–39].

As a result, the differences with respect to the MEaSUREs velocities are on the order of a few centimeters/day, and the angular direction is consistent with the geomorphological control given by the main direction of the glacier flow (Figure 8).

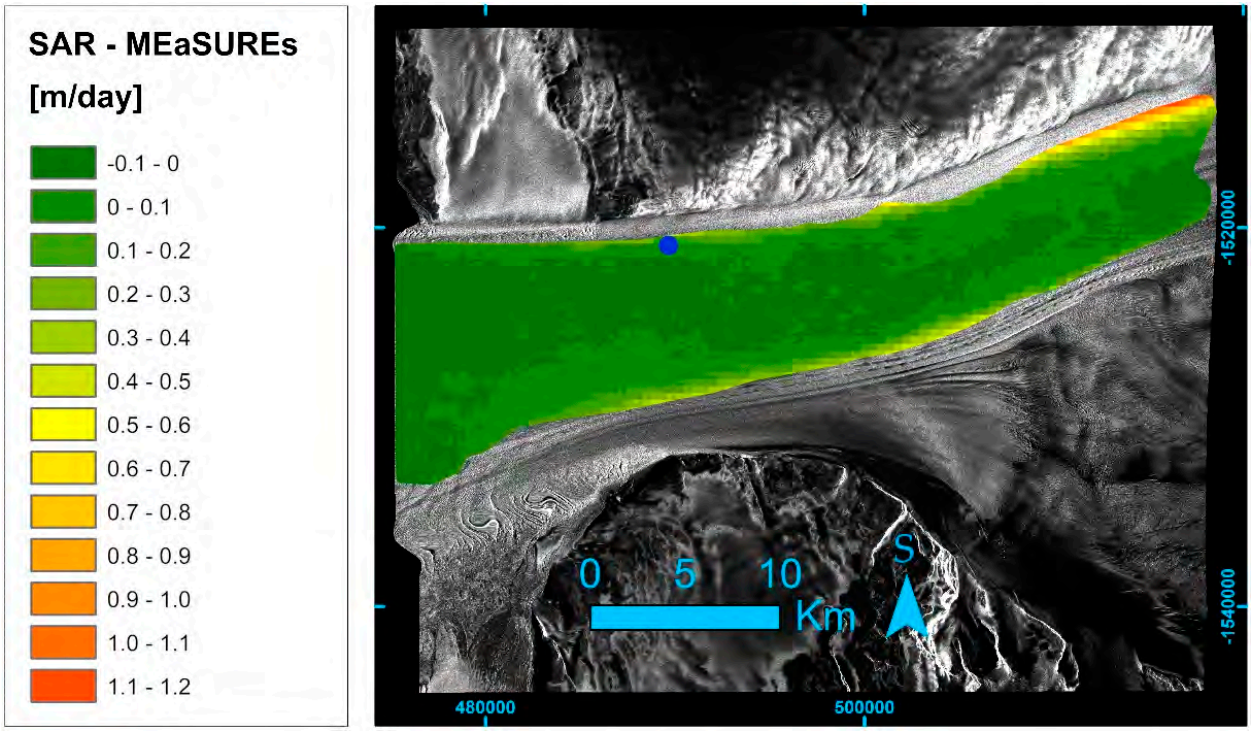

Figure 8. Differences between the horizontal daily velocities of SAR pair 1 and the ones of the MEaSUREs InSAR-Based Antarctica Ice Velocity Map, Version 2. The blue dot corresponds to the position of DRY1 GPS point. Coordinates are expressed in Antarctic Polar Stereographic mapping projection.

Moreover, the offset tracking velocities of the three SAR pairs were also validated with respect to the DRY1 GNSS point, as shown in the Table 4.

Table 4. Comparison between the horizontal velocity, and its components, of the DRY1 GNSS point, and the interpolated offsets of the three processed SAR pairs. Values are expressed in meters per day.

Components	Dry1 (m/day)	SAR p.I (m/day)	SAR p.II (m/day)	SAR p.III (m/day)
Ven	1.489	1.509	1.502	1.508
Ve	1.461	1.480	1.473	1.479
Vn	−0.288	−0.293	−0.292	−0.293

In Figure 9a–c are reported the estimated horizontal velocities derived by interpolating the SAR offset tracking values of the three pairs, along with the predicted ocean tide in the period corresponding to the acquisition of the master and slave scene of each image pair.

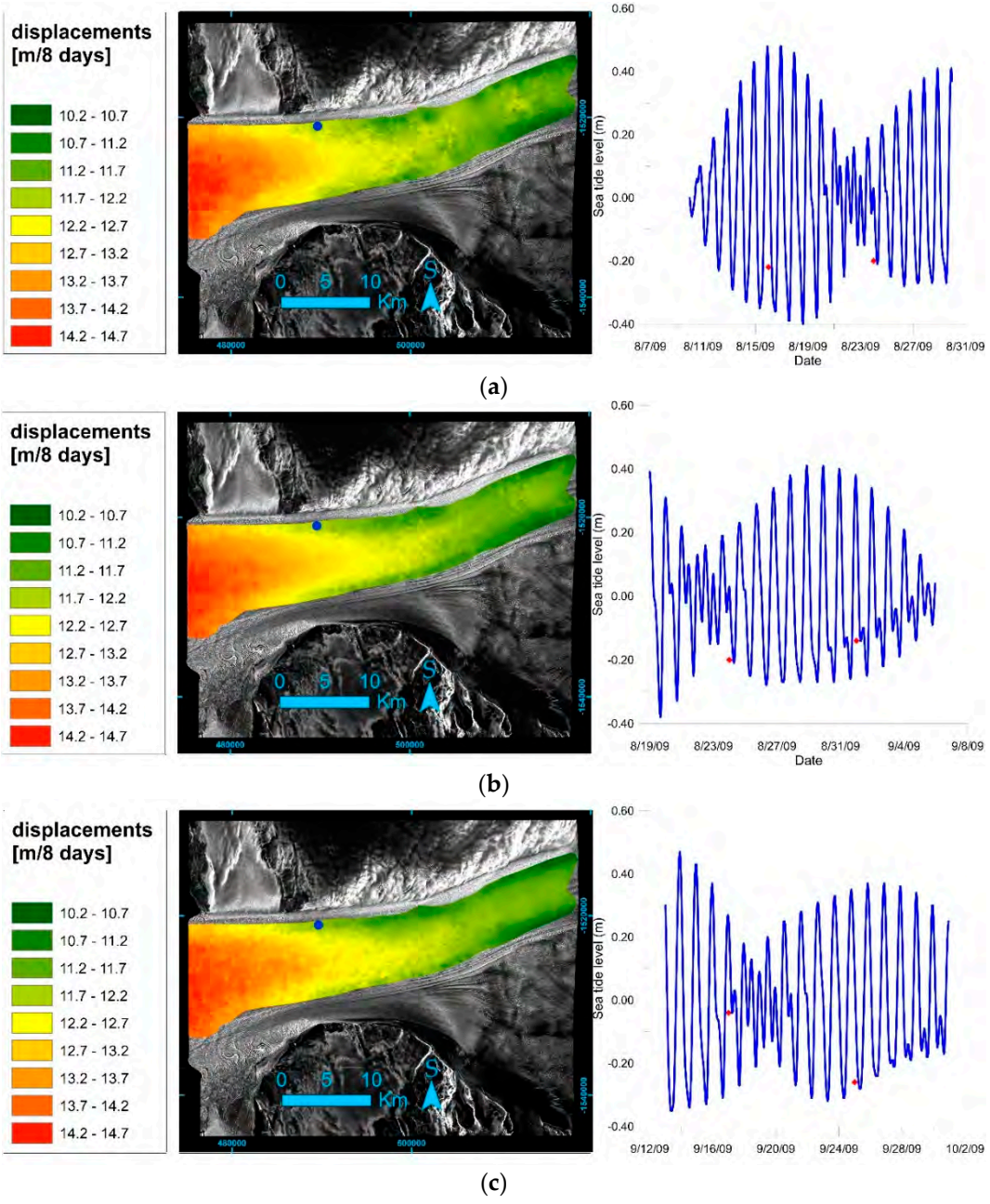

Figure 9. On the left, grids obtained interpolating the horizontal component of the offset points on the floating part of southern flux of the David Glacier, from top to bottom, respectively, pair I (**a**), pair II (**b**), and pair III (**c**). The blue dot corresponds to the position of DRY1 GPS point. Coordinates are expressed in Antarctic Polar Stereographic mapping projection. On the right are graphs reporting the timing of SAR image acquisition with respect to the predicted ocean tide variations. The red dots in the graphs correspond to the master and slave scenes of the three image-pairs.

4. Results

The three components of the position, obtained from PPP solutions, show different trends. While the Up component of DRY1 shows a clear periodicity quite similar with predicted ocean tide series (Figure 6), the Up component of ICF1 station shows a very small ocean tidal response and highlights the elevation changes due to the ice flow through the complex area of the curved path of the David Cauldron neck.

The reduction in the amplitude of oscillation of DRY1 with respect to the predicted ocean tide at MZS (100 km northward) is confirmed even by observing the expected

amplitude of ocean tide at Cape Roberts, about 170 km southward of DRY1, excluding an effect due to the geographical position of DRY1 within the Ross Sea. The high correlation of the phase of ocean tide response of the ice tongue with respect to forecast signals can be directly observed in Figure 7. The DRY1 station is located about 40 km seaward with respect to the estimated position of the grounding zone; considering the elevation of the point above sea level, the submerged thickness of the ice is roughly 600 m at the DRY1 position. The reduction in the amplitude of the observed ice tide at DRY1 could be explained by ice thickness and lateral friction with respect to the rocky walls in which it expands inside a fjord.

The Lomb–Scargle periodograms shown in Figure 6 show that:

- The DRY1 series (Figure 6A) shows three significant periodicities, only in the UP component (Table 2, Figure 7), corresponding to amplitudes of 12.6 cm (T1), 12.3 cm (T2), and 7.9 cm (T3). However, the ICF1 series (Figure 6B) shows no significant periodicity in the three components.
- The peaks of the predicted ocean tide T1 and T2 series correspond to those of the DRY1 series T2 and T1. They have slightly greater amplitudes and similar periods whose differences fall within the 10 min.

Analyzing the daily scale series (Figure 10), at the maximum ocean tide amplitude, the GNSS station DRY1 presents a delay of about 3 h before responding to the lowering of the ocean tide. ICF1 also records a very small tidal signal, in phase with the predicted one, with the same delay.

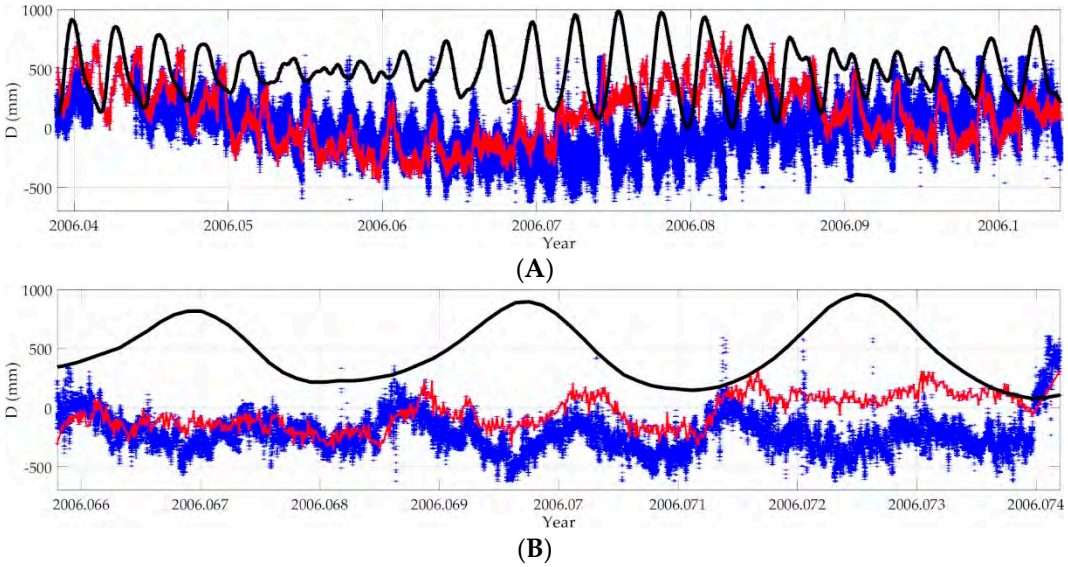

Figure 10. DRY1 East (**red**) and North (**blue**) components with respect to the predicted tide signal (**black**); (**A**) whole series, (**B**) a detail around tide daily signals.

To highlight some correspondence between the surface morphology and the survey carried out at sites, comparisons were made with the Reference Digital Elevation Model of Antarctica REMA [40] along the profiles having the same horizontal directions as the control point (Figure 11).

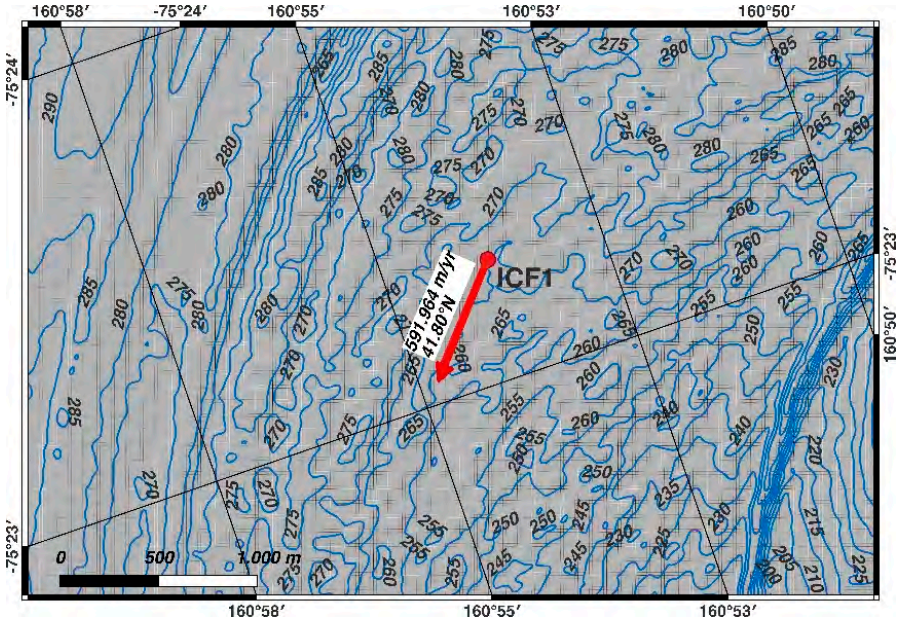

(**A**)

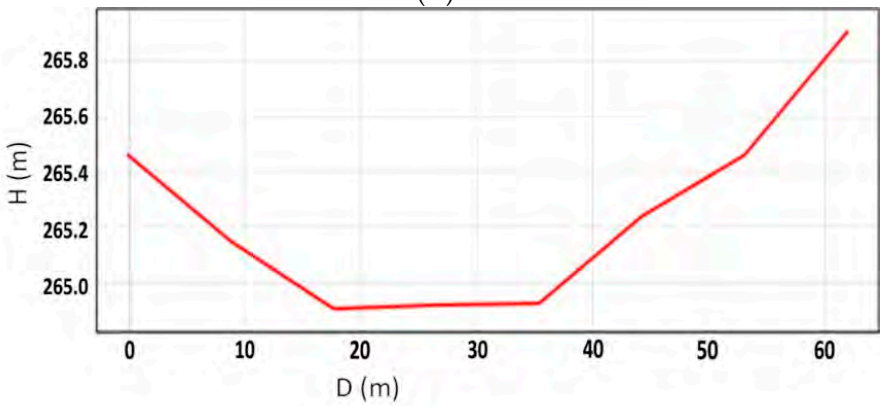

(**B**)

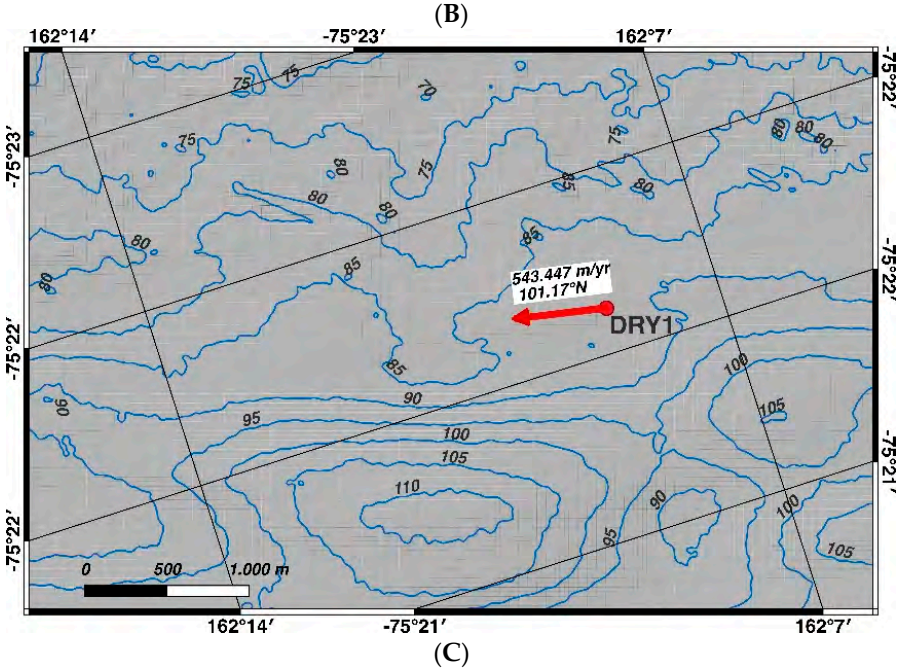

(**C**)

Figure 11. *Cont.*

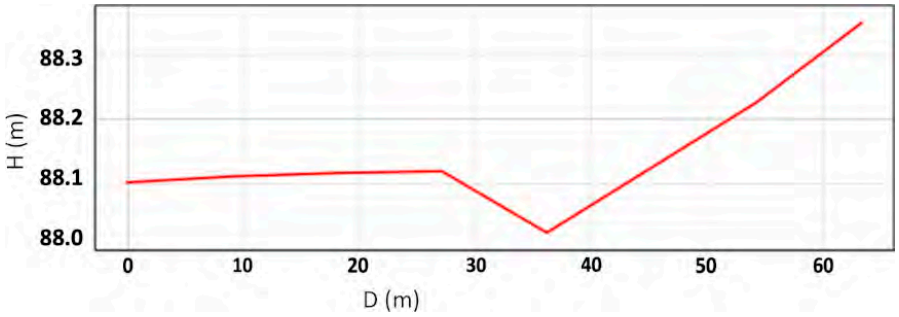

(**D**)

Figure 11. DTM extracted from REMA [40]. The red arrows of figure (**A**,**C**) represent the 2D rate of movements shown in Table 1 (ICF1, 591.964 m/yr; DRY1, 543.447 m/yr); (**B**,**D**) are REMA vertical profiles from the line of movements with azimuth 41.80°N (ICF1) and 101.17°N (DRY1).

5. Discussion

The analysis of the time series of the two GNSS stations can provide useful information on the movements of floating and grounded parts of David Glacier, both considering the total analyzed period and a daily scale. From the time series shown in Figures 3 and 4, the two GNSS stations have significantly different oscillatory movements due to the locations of the two stations on the glacial tongue with respect to the grounding zone. The DRY1 station points out a horizontal velocity slower than the ICF1 (respectively, 543.447 m/yr $\pm$ 0.026 m/yr and 591.964 m/yr $\pm$ 0.021 m/yr), and it shows a clear vertical ocean tide signal, but with reduced amplitude, when compared with the predicted one at the same location. ICF1 shows a very small tidal signal at the daily scale in the three components and shows a clear change of horizontal ice flow direction following the constraints of the fjord geometry. A possible explanation for the "saddle" vertical behavior of the point, compared with the local slope of REMA, is that the ice flow from the plateau could encounter a morphological change in the bedrock interface.

In the paper Frezzotti et al. [39], the velocities measured in the period December 1991–January/February 1994 of a series of points surveyed using GNSS are reported. One of these points (DA2) was in 1994 at a distance of 135.55 m from point DRY1, with an azimuth almost transversal to the point analyzed in this paper (92.47°N). In the period 1991–1994, the published velocity was 533.38 m/yr with an azimuth of 101° against values measured in 2006 through the analysis described here of 543.447 m/yr with an azimuth of 101.17°N. As can be seen, the direction has remained almost constant, although, in the first case, the velocity was averaged over several years in different seasons, and the velocity was higher than 10.07 m/yr in Antarctic summer 2006 with respect to the velocity during 1991–1994. It is not possible from the dataset analyzed in this context alone to understand whether it is a seasonal variation or an overall increase in meridional ice flow velocity, and further measurements would be required.

The ice tongue flows essentially along an E-SE direction; DRY1 shows daily East and North components in phase opposition with respect to the Up component (Figure 4). The rising of the ocean tide even increases the movement component of DRY1 orthogonal to the main flow direction, which cannot be explained simply by a vertical oscillation of the aluminum pole caused by a transversal change in the glacier slope. In fact, the effects are greater than what might be expected if there were a lateral constraint caused by the anchoring of the ice to the fjord wall and a free vertical oscillation due to ocean tide in the floating part of the tongue, considering the arm of the GNSS antenna pole as leverage. For example, starting from the behavior of the component orthogonal to the ice flow at DRY1 described in Figure 4, during the maximum tidal excursions, the horizontal variation orthogonal to the flow is about $\pm$6 cm; considering the height of the pole of about 2 m out from the ice, in the case of a rotation instead of a horizontal movement, the effects should require a rotation of the ice surface of about $\pm 2^{\circ}$, which, even in presence of fractured ice blocks of a few hundred meters, would require ocean tidal excursions of several meters.

During the phase of greatest tidal excursion (14-day period), an increase in the horizontal ice flow following an increase in the ocean tide amplitude can be observed, but, at daily level, the maximum horizontal velocity it is often observed during the low-tide phase; this effect is in accordance with the direction of seawater outflow from the fjord into the ocean and could also be linked to the constraints of the ice flow driven by gravity [41–43].

Analyzing the horizontal velocities at ICF1 and DRY1, a sinusoidal residual signal is highlighted in the detrended time series of movement differences, which could be induced by the torsional motion of the ice flow due to the outflow from the neck of fjord at ICF1 and by the strong confinement induced at DRY1 by the pressure of the northern stream fed by the Talos Dome.

Concerning the SAR data processing, even though the scenes were all acquired at the same time, about 06:15 UTC, corresponding to a low tide condition, their position in the tidal cycle is different, as shown in Figure 9.

This means that, at the time of the SAR scene acquisition, the glacier is always grounded, but in the time span between on acquisition and another one, its floating time varies depending upon tidal conditions. Starting from this consideration, it is possible to hypothesize that, in the time span corresponding to the temporal baseline of the SAR pairs, the horizontal velocity of the glacier should be greater when the glacier remains floating for longer, since high tide tends to uplift the glacier from the bedrock, and so, due to decreasing basal friction, its horizontal velocity increases. To check this hypothesis, we compared the high tide total height with respect to the summation of horizontal displacements. The high tide total height was calculated with the Cavalieri-Simpson formula [44] applied to predicted ocean tide at the DRY1 point location; in other words, the analysis corresponds to the mathematical integration of the height in every positive tide condition. A positive correlation between tide heights and velocity becomes clear starting from a tide threshold of 10 cm above the sea level (Figure 12).

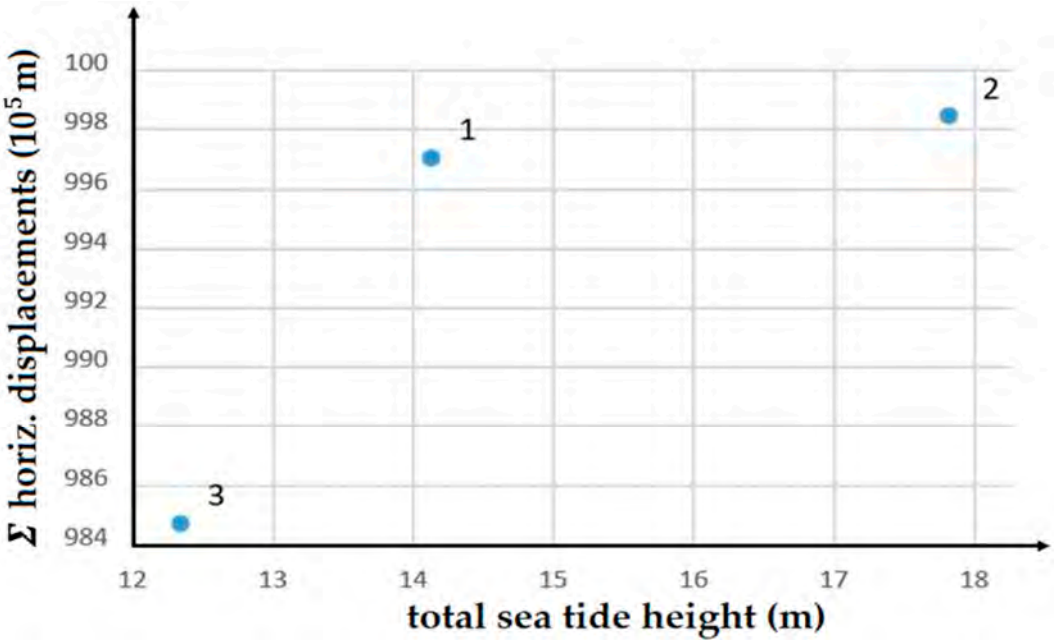

Figure 12. Chart between total ocean tide height (abscissa) and summation of horizontal displacements (ordinate), considering a threshold of 10 cm upon sea level. Here, displacement summation refers to the whole region of the glacier included in the SAR scenes. The numbers beside the dots refer to the SAR pairs.

This correlation is verified both for the whole glacier region included in the SAR scenes and for an area of 12 km surrounding the point DRY1. Unfortunately, the few numbers of

processed SAR pairs allow neither deriving a conclusion nor attempting a correlation with the GNSS time series.

6. Conclusions

The Drygalski ice tongue interacts with the southern coast of Terra Nova Bay and has an important role in the formation of the polynya, resulting from the action of strong persistent katabatic winds which inhibit the formation of sea ice in the bay and, at the same time, induce the ice formation process beyond this area due to persistent cooling of the water surface [42]. In addition, Drygalski, with its giant length towards the sea, forms a physical obstacle to the entry of sea ice into Terra Nova Bay from the south. Various authors, e.g., [3,7,11], observed that, even in the presence of a strongly segmented surface of the floating tongue, the main calving events are of large dimension, also connected to collisions with big icebergs (such as B15A) which significantly affect the tongue length. Precise measurements of ice flow velocities are particularly useful for understanding the equilibrium length of the tongue itself. Among these, geodetic GNSS measurements are the best ground truth constraints to be used for surveys extended at the areal level, conducted with remote sensing techniques such as satellite image feature tracking or SAR interferometry.

The analysis of the time series of the GNSS stations DRY1 and ICF1 has highlighted different behaviors, strictly dependent on their position on the ice tongue with respect to the grounding zone, the ocean tides, the morphology of the bedrock, and the fjord geometry. In general, the main daily signal is related to the tidal constraint, which produces changes in the ice flow velocities inversely proportional to its amplitude. During low tide, the velocity of the ice flow reaches its daily maximum, in accordance with the direction of seawater outflow from the fjord into the ocean. In contrast, the inflow of sea water during the rising of the ocean tide level is characterized by an opposite movement to the outflow of the ice towards the sea. During the phase of greatest daily tidal excursion, an increase in the horizontal ice flow velocity can be observed. This could be explained by longer periods of seawater presence at the bedrock-ice interface in the grounding zone, with respect to the phases of small daily ocean tidal excursions.

DRY1 demonstrates a clear response of the floating ice tongue to tidal forces, while ICF1, located close to the grounding zones, shows a very limited daily vertical amplitude of movements induced by the ocean tide.

The small oscillating components observed within the southern flow in a transversal direction with respect to the main longitudinal flow is not easily interpretable on the basis of only 24 days of GNSS observation and would require a longer acquisition at different points of the David Glacier and the Drygalski ice tongue to identify the principal causes of what was observed.

All processed SAR scenes were acquired at the same daily time, corresponding to the low-tide condition, in which the threshold of the grounding zone is supposed to lean against the bedrock. However, in the time span between scene acquisitions there were also tidal peaks, which facilitate the movements of the glacier. The comparison between the integral of tide height computed over an 8-day period against the summation of the horizontal displacements obtained by SAR offset tracking shows a positive correlation becoming clear from 0.1 m above sea level, while below this threshold it is assumed that the movement of the glacier is constrained.

In particular, the DRY1 GNSS time series highlights that, on a daily basis, the horizontal velocity of the pole on which the antenna was positioned increases in correspondence (with a delay of about 3 h) with low tide conditions, in accordance with the direction of seawater outflow from the fjord into the ocean and with a topographic gradient effect, while the SAR processing shows that, over an 8-day period, the overall horizontal velocity of the acquired portion of the glacier increases when it is released from the bedrock, i.e., in tidal conditions higher than a threshold of 10 cm above the sea level.

The variations in the strain pattern of the floating ice tongues can be induced by the formation of basal channels which are also located on the lower side of the David Drygalski [3]. These channels can be explained by increased melting at the ice-ocean interface [45–48], and in some cases subglacial channel outflow can go beyond the grounding line [12,48].

Chen et al. [49], reveals a complex model for the definition of grounding line, which is inconsistent in position with respect to simple tidal forcing and which presents migrations of the grounding line within a large grounding zone. This phenomenon is influenced by numerous factors, including, for example, the hardness of the bed and the presence of subglacial channels. Given that, for the David-Drygalski, as previously indicated, at least three main subglacial channels have been identified, there could be a phenomenon of inland sea water trapping. Even in this area, the position of the grounding line should perhaps be assumed not to be fixed. But to deepen this aspect for the grounding zone of the David Drygalski, further investigations would be necessary, through long time series of altimetric data straddling the grounding zone.

The position of the GNSS points ICF1 and DRY1 is lateral southward, in a higher altimetric position based on the description provided by the DEM REMA, with respect to the three subglacial channels identified in Indrigo [3]. Two of these are located within the southern flow of David Glacier, and it has been hypothesized that they may reach the grounding line. In this case, the inflow and outflow induced by tidal level variations, which leads to the observation of significant surface velocity variation signals measured daily at the GNSS points, could have reciprocal correlations with the presence of the two subglacial channels.

Author Contributions: L.V. and A.Z. conceived and designed the paper; M.D., L.V. and A.Z. joined in Antarctic Scientific Expeditions; A.L. and L.V. analyzed the SAR data; L.M., L.V. and A.Z. analyzed the GNSS data; A.L, L.V. and A.Z. developed the glaciological interpretation of the data results; A.L., L.M., L.V. and A.Z. contributed to the writing of the paper. All authors have read and agreed to the published version of the manuscript.

Funding: This work was conducted with field logistical and financial support provided by the Italian National Program for Antarctic Research (PNRA 2004/2.05) funded by the Italian Ministry of Research (MUR).

Data Availability Statement: Not applicable.

Acknowledgments: The personnel of Mario Zucchelli Station which supported the logistics of the surveys.

Conflicts of Interest: The authors declare no conflict of interest.

References

1. Rignot, E. Mass balance of East Antarctic glaciers and ice shelves from satellite data. *Ann. Glaciol.* **2002**, *34*, 217–227. [CrossRef]
2. Frezzotti, M.; Tabacco, I.E.; Zirizzotti, A. Ice discharge of eastern Dome C drainage area, Antarctica, determined from airborne radar survey and satellite image analysis. *J. Glaciol.* **2000**, *46*, 253–264. [CrossRef]
3. Indrigo, C.; Dow, C.F.; Greenbaum, J.S.; Morlighem, M. Drygalski Ice Tongue stability influenced by rift formation and ice morphology. *J. Glaciol.* **2020**, *67*, 243–252. [CrossRef]
4. Bindschadler, R.; Choi, H.; Wichlacz, A.; Bingham, R.; Bohlander, J.; Brunt, K.; Corr, H.; Drews, R.; Fricker, H.; Hall, M.; et al. Getting around Antarctica: New high-resolution mappings of the grounded and freely-floating boundaries of the Antarctic ice sheet created for the International Polar Year. *Cryosphere* **2011**, *5*, 569–588. [CrossRef]
5. Stearns, L.A. Dynamics and mass balance of four large East Antarctic outlet glaciers. *Ann. Glaciol.* **2011**, *52*, 116–126. [CrossRef]
6. Frezzotti, M. Glaciological study in Terra Nova Bay, Antarctica, inferred from remote sensing analysis. *Ann. Glaciol.* **1993**, *17*, 63–71. [CrossRef]
7. Frezzotti, M.; Mabin, M.C.G. 20th century behavior of Drygalski Ice Tongue, Ross Sea. *Antarct. Ann. Glaciol.* **1994**, *20*, 397–400. [CrossRef]
8. Frezzotti, M. Ice front fluctuation, iceberg calving flux and mass balance of Victoria Land glaciers. *Antarct. Sci.* **1997**, *9*, 61–73. [CrossRef]
9. Rignot, E.; Mouginot, J.; Scheuchl, B.; Broeke, M.V.D.; van Wessem, M.J.; Morlighem, M. Four decades of Antarctic Ice Sheet mass balance from 1979–2017. *Proc. Natl. Acad. Sci. USA* **2019**, *116*, 1095–1103. [CrossRef]

10. Tabacco, I.E.; Bianchi, C.; Chiappini, M.; Zirizzotti, A.; Zuccheretti, E. Analysis of bottom morphology of the David Glacier-Drygalski Ice Tongue, East Antarctica. *Ann. Glaciol.* **2000**, *30*, 47–51. [CrossRef]
11. Wuite, J.; Jezek, K.C.; Wu, X.; Farness, K.; Carande, R. The velocity field and flow regime of David Glacier and Drygalski Ice Tongue, Antarctica. *Polar Geogr.* **2009**, *32*, 111–127. [CrossRef]
12. Le Brocq, A.M.; Ross, N.; Griggs, J.A.; Bingham, R.G.; Corr, H.F.J.; Ferraccioli, F.; Jenkins, A.; Jordan, T.A.; Payne, A.J.; Rippin, D.M.; et al. Evidence from ice shelves for channelized meltwater flow beneath the Antarctic Ice Sheet. *Nat. Geosci.* **2013**, *6*, 945–948. [CrossRef]
13. Rignot, E.; Mouginot, J.; Scheuchl, B. *MEaSUREs InSAR-Based Antarctica Ice Velocity Map, Version 2*; Distributed Active Archive Center, NASA National Snow and Ice Data Center: Boulder, CO, USA, 2017. [CrossRef]
14. Moon, J.; Cho, Y.; Lee, H. Flow Velocity Change of David Glacier, East Antarctica, from 2016 to 2020 Observed by Sentinel-1A SAR Offset Tracking Method. *Korean J. Remote Sens.* **2021**, *37*, 1–11. [CrossRef]
15. Stutz, J.; Mackintosh, A.; Norton, K.; Whitmore, R.; Baroni, C.; Jamieson, S.S.R.; Jones, R.S.; Balco, G.; Salvatore, M.C.; Casale, S.; et al. Mid-Holocene thinning of David Glacier, Antarctica: Chronology and controls. *Cryosphere* **2021**, *15*, 5447–5471. [CrossRef]
16. Danesi, S.; Salimbeni, S.; Borghi, A.; Urbini, S.; Frezzotti, M. Cryo-seismicity triggered by ice mass discharge through the Antarctic subglacial hydrographic network. *EGUsphere*, 2022, *preprint*. [CrossRef]
17. Vittuari, L.; Dubbini, M.; Martelli, L.; Zanutta, A. Sea Tide Analysis Derived by PPP Kinematic GPS Data Acquired at David-Drygalski Floating Ice Tongue (Antarctica). In *R3 in Geomatics: Research, Results and Review. R3GEO 2019. Communications in Computer and Information Science*; Parente, C., Troisi, S., Vettore, A., Eds.; Springer International Publishing: Cham, Switzerland, 2020; pp. 142–154. [CrossRef]
18. Rignot, E.; Mouginot, J.; Scheuchl, B. Ice Flow of the Antarctic Ice Sheet. *Science* **2011**, *333*, 1427–1430. [CrossRef]
19. Rignot, E.; Mouginot, J.; Morlighem, M.; Seroussi, H.; Scheuchl, B. Widespread, rapid grounding line retreat of Pine Island, Thwaites, Smith, and Kohler glaciers, West Antarctica, from 1992 to 2011. *Geophys. Res. Lett.* **2014**, *41*, 3502–3509. [CrossRef]
20. Rignot, E.; Mouginot, J.; Scheuchl, B. *MEaSUREs Antarctic Grounding Line from Differential Satellite Radar Interferometry, Version 2*; Distributed Active Archive Center, NASA National Snow and Ice Data Center: Boulder, CO, USA, 2016. [CrossRef]
21. Danesi, S.; Dubbini, M.; Morelli, A.; Vittuari, L.; Bannister, S. Joint Geophysical Observations of Ice Stream Dynamics. In *Geodetic and Geophysical Observations in Antarctica*; Springer: Berlin/Heidelberg, Germany, 2008; pp. 281–298. [CrossRef]
22. Dach, R.; Lutz, S.; Walser, P.; Fridez, P. *Bernese GNSS Software Version 5.2*; User Manual; Astronomical Institute, University of Bern, Bern Open Publishing: Bern, Switzerland, 2015; ISBN 978-3-906813-05-9. [CrossRef]
23. King, M. Tidal observations on floating ice using a single GPS receiver. *Geophys. Res. Lett.* **2003**, *30*. [CrossRef]
24. Petit, G.; Luzum, B. The 2010 Reference Edition of the IERS Conventions. In *Reference Frames for Applications in Geosciences*; Altamimi, Z., Collilieux, X., Eds.; Springer: Berlin/Heidelberg, Germany, 2012; pp. 57–61. [CrossRef]
25. Herring, T. MATLAB Tools for viewing GPS velocities and time series. *GPS Solut.* **2003**, *7*, 194–199. [CrossRef]
26. Dawidowicz, K. Analysis of PCC model dependent periodic signals in GLONASS position time series using Lomb_Scargle periodogram. *Acta Geodyn. Geomater.* **2016**, 299–314. [CrossRef]
27. Lomb, N.R. Least-squares frequency analysis of unequally spaced data. *Astrophys. Space Sci.* **1976**, *39*, 447–462. [CrossRef]
28. Scargle, J.D. Studies in astronomical time series analysis. II - Statistical aspects of spectral analysis of unevenly spaced data. *Astrophys. J.* **1982**, *263*, 835–853. [CrossRef]
29. Vanderplas, J.T. Understanding the Lomb–Scargle Periodogram. *Astrophys. J. Suppl. Ser.* **2018**, *236*, 16. [CrossRef]
30. Shumway, R.H.; Stoffer, D.S. *Time Series Analysis and Its Applications*; Springer: New York, NY, USA, 2000. [CrossRef]
31. Thiel, E.; Crary, A.P.; Haubrich, R.A.; Behrendt, J.C. Gravimetric determination of ocean tide, Weddell and Ross seas, Antarctica. *J. Geophys. Res. Atmos.* **1960**, *65*, 629–636. [CrossRef]
32. Lescarmontier, L.; Legrésy, B.; Coleman, R.; Perosanz, F.; Mayet, C.; Testut, L. Vibrations of Mertz Glacier ice tongue, East Antarctica. *J. Glaciol.* **2012**, *58*, 665–676. [CrossRef]
33. Strozzi, T.; Luckman, A.; Murray, T.; Wegmuller, U.; Werner, C. Glacier motion estimation using SAR offset-tracking procedures. *IEEE Trans. Geosci. Remote Sens.* **2002**, *40*, 2384–2391. [CrossRef]
34. Nitti, D.O.; Hanssen, R.F.; Refice, A.; Bovenga, F.; Milillo, G.; Nutricato, R. Evaluation of DEM-assisted SAR coregistration. In *Image and Signal Processing for Remote Sensing XIV*; SPIE: Bellingham, WA, USA, 2008; Volume 7109, p. 710919. [CrossRef]
35. Liu, H.; Zhao, Z.; Jezek, K.C. Synergistic Fusion of Interferometric and Speckle-Tracking Methods for Deriving Surface Velocity From Interferometric SAR Data. *IEEE Geosci. Remote Sens. Lett.* **2007**, *4*, 102–106. [CrossRef]
36. Kwok, R.; Fahnestock, M. Ice sheet motion and topography from radar interferometry. *IEEE Trans. Geosci. Remote Sens.* **1996**, *34*, 189–200. [CrossRef]
37. Mouginot, J.; Scheuchl, B.; Rignot, E. Mapping of Ice Motion in Antarctica Using Synthetic-Aperture Radar Data. *Remote Sens.* **2012**, *4*, 2753–2767. [CrossRef]
38. Frezzotti, M.; Capra, A.; Vittuari, L. Comparison between glacier ice velocities inferred from GPS and sequential satellite images. *Ann. Glaciol.* **1998**, *27*, 54–60. [CrossRef]
39. Mouginot, J.; Rignot, E.; Scheuchl, B.; Millan, R. Comprehensive Annual Ice Sheet Velocity Mapping Using Landsat-8, Sentinel-1, and RADARSAT-2 Data. *Remote Sens.* **2017**, *9*, 364. [CrossRef]
40. Howat, I.M.; Porter, C.; Smith, B.E.; Noh, M.-J.; Morin, P. The Reference Elevation Model of Antarctica. *Cryosphere* **2019**, *13*, 665–674. [CrossRef]

41. Makinson, K.; Holland, P.R.; Jenkins, A.; Nicholls, K.W.; Holland, D.M. Influence of tides on melting and freezing beneath Filchner-Ronne Ice Shelf, Antarctica. *Geophys. Res. Lett.* **2011**, *38*. [CrossRef]
42. Stevens, C.; Lee, W.S.; Fusco, G.; Yun, S.; Grant, B.; Robinson, N.; Hwang, C.Y. The influence of the Drygalski Ice Tongue on the local ocean. *Ann. Glaciol.* **2017**, *58*, 51–59. [CrossRef]
43. Stevens, C.; Hulbe, C.; Brewer, M.; Stewart, C.; Robinson, N.; Ohneiser, C.; Jendersie, S. Ocean mixing and heat transport processes observed under the Ross Ice Shelf control its basal melting. *Proc. Natl. Acad. Sci. USA* **2020**, *117*, 16799–16804. [CrossRef]
44. Velleman, D.J. The Generalized Simpson's Rule. *Am. Math. Mon.* **2005**, *112*, 342–350. [CrossRef]
45. Rignot, E.; Steffen, K. Channelized bottom melting and stability of floating ice shelves. *Geophys. Res. Lett.* **2008**, *35*. [CrossRef]
46. Pritchard, H.D.; Ligtenberg, S.R.M.; Fricker, H.A.; Vaughan, D.G.; Broeke, M.R.V.D.; Padman, L. Antarctic ice-sheet loss driven by basal melting of ice shelves. *Nature* **2012**, *484*, 502–505. [CrossRef]
47. Vaughan, D.G.; Corr, H.F.J.; Bindschadler, R.A.; Dutrieux, P.; Gudmundsson, G.H.; Jenkins, A.; Newman, T.; Vornberger, P.; Wingham, D.J. Subglacial melt channels and fracture in the floating part of Pine Island Glacier, Antarctica. *J. Geophys. Res. Atmos.* **2012**, *117*. [CrossRef]
48. Alley, K.E.; Scambos, T.A.; Siegfried, M.R.; Fricker, H.A. Impacts of warm water on Antarctic ice shelf stability through basal channel formation. *Nat. Geosci.* **2016**, *9*, 290–293. [CrossRef]
49. Chen, H.; Rignot, E.; Scheuchl, B.; Ehrenfeucht, S. Grounding Zone of Amery Ice Shelf, Antarctica, from Differential Synthetic-Aperture Radar Interferometry. *Geophys. Res. Lett.* **2023**, *50*, e2022GL102430. [CrossRef]